IN-71-TM

CEAS
AAAF · AIAE · AIDAA
DGLR · NVvL · RAeS

AIAA
American Institute of
Aeronautics and Astronautics

FIRST JOINT CEAS/AIAA
AEROACOUSTICS CONFERENCE
(16th AIAA Aeroacoustics Conference)

12 - 15 June, 1995
München Penta Hotel, Munich, Germany

CEAS/AIAA-95-149

Nozzle Thrust Optimization While Reducing Jet Noise

J. M. Seiner
M. M. Gilinsky

NASA Langley Research Center
Hampton, Virginia, USA

NOZZLE THRUST OPTIMIZATION WHILE REDUCING JET NOISE

Seiner J.M[†] , **Gilinsky M.M.**[*]

NASA Langley Research Center

Hampton, VA 23681

ABSTRACT

A Bluebell nozzle design concept is proposed for jet noise reduction with minimal thrust loss or even thrust augmentation. A "Bluebell nozzle" [1] has a sinusoidal lip line edge (chevrons) and a sinusoidal cross section shape with linear amplitude increasing downstream in the divergent nozzle part (corrugations). The experimental tests of several Bluebell nozzle designs have shown noise reduction relative to a convergent-divergent round nozzle with design exhaust Mach number $M_e = 1.5$. The best design provides an acoustic benefit near 4dB with about 1% thrust augmentation. For subsonic flow ($M_e = 0.6$) the tests indicated that the present method for design of Bluebell nozzles gives less acoustic benefit and in most cases jet noise increased.

The proposed designs incorporate analytical theory and 2D and 3D numerical simulations. Full Navier-Stokes and Euler solvers were utilized. Boundary layer effects were used. Several different designs were accounted for in the Euler applications.

INTRODUCTION

Successful design of a nozzle system for supersonic commercial aircraft involves meeting both environmental and economic metrics. For nozzles, the environmental metric is noise, as expressed in the FAR 36 Stage III regulations. Economic metrics are usually associated with both take-off and cruise aeroperformance, weight, mechanical complexity, and structural reliability. These very involved issues are beyond the scope of this paper, but there exist fundamental considerations involving implementation of both metrics that are the subject of this paper.

Several years ago it became apparent that a program was required that placed more emphasis on scientific methods for the design of nozzles for supersonic commercial applications. Current methods heavily rely on state-of-the-art empirical methods that are supported by massive data sets from prior nozzle testing. The process is both cumbersome and expensive. Examples of this can be found in a review article by Seiner and Krejsa [2]. The most successful nozzle designs are based on nozzle geometry that controls the strength of shock waves, that can rapidly mix high and low speed streams efficiently, and produce noise spectrally outside the range of the Noy weighting. One discovers very quickly, however, that real solutions can only be achieved with a nozzle concept that is still effective at reducing noise at low jet exhaust velocities, where trades with nozzle performance are historically disappointing to date. Subsonic jet noise reduction represents a fine example of this point, where noise reduction is achieved primarily through increase of engine by-pass ratio which leads to low mixed flow velocities. For supersonic aircraft, it is unknown if an economic solution exists for high by-pass ratio engines.

One simple, yet realistic, question to pose is what technology exists that can optimize both the aeroacoustic suppression characteristics and suppressed mode performance of any given nozzle design. One would, in particular, like to know this for nozzles targeted to operate with low jet exhaust velocities. One cannot, of course, directly answer this question. We can, however, outline aspects of this technology. For example, in the lobed mixer of Presz [3], counter-rotating axial vorticity generated by mixer lobes is used to mix high speed engine primary core and fan stream flow with entrained lower speed secondary flow from an ejector inlet. The enhanced mixing is used to both increase the level of secondary flow entrainment and mix high and low stream flow to achieve lower speed uniform ejector exit velocity that has an acceptable level of external jet noise. The current state-of-the-art cannot adequately relate the design of lobe geometry to prediction of circulation strength of counter-rotating vorticity nor can it determine the circulation strength required to achieve full mixing in the shortest possible ejector duct. Additionally, both aeroperformance computations and nozzle internal noise computations cannot be treated with sufficient accuracy to optimize the design. Similar observations of nozzle suppression effectiveness can be made for other nozzle concepts, like those previously discussed in reference [2].

The approach described in the present paper attempts to develop a process involving optimal design of noise suppression technology for both subsonic and supersonic applications. As such, it is not necessary that

---

[†] Senior Research Scientist, Associate Fellow AIAA

[*] Senior Research Associate, NRC, Member AIAA

we even consider nozzle geometry that meets any particular international noise regulation when projected to product scale. It is sufficient that the nozzle geometry selected contains one or several concepts that achieve some level of noise reduction. The long term objective of the research is to explain observed noise reduction from alteration of the turbulent source function and relate this to the nozzle geometry for optimization. Toward this purpose, we have selected a simple axisymmetric nozzle geometry (see Figure 1), which we denote as a Bluebell nozzle due to the observed petal shapes of the nozzle plume generated by this nozzle. The Bluebell nozzle utilizes two concepts that have been used in the past to suppress noise. These concepts involve the use of chevrons to enhance the nozzle exit perimeter to increase the area for mixing and internal corrugations to generate counter-rotating axial vorticity to enhance mixing of high speed primary flow with low speed secodary flow. The present research does not yet include an ejector.

Several Bluebell nozzles have been constructed with select variations of the chevron and corrugation geometry. All of these were designed as convergent-divergent nozzles for an exit Mach number of 1.5. In this paper predictions of thrust and measurement of the noise are made to enable optimization of the nozzle geometry. The intermediate steps, of either numerical simulation or measurement of the turbulence with consequent prediction of the noise, remains a deficiency of the present paper, but is being addressed in future work. The thrust calculations were performed in both 2D and 3D using the Krayko-Godunov first order numerical scheme (K-G-code) with and without boundary layer corrections. In select cases a full Navier-Stokes code with k-ε turbulence model, the CRAFT code, was also applied to evaluate performance based calculations when a boundary layer correction was applied to an Euler analysis (K-G-code). Acoustic measurements were acquired on baseline reference nozzles and all Bluebell nozzles. The results, as presented below, demonstrate that it is possible to achieve a level of optimal nozzle design through consideration of both performance and noise reduction.

A BLUEBELL NOZZLE.

1. NOZZLE GEOMETRY.

The proposed Bluebell nozzle can be constucted on the base of any plain nozzle: axisymmetric round conical, elliptical, triangular, rectangular, 2D-CD plane. Let us consider the axisymmetric baseline nozzle contour, which is described by the function $R = R_o(x)$ in a meridional plane φ =const. For the Bluebell nozzle the function $R_n(x)$ describes the nozzle geometry. The convergent part is represented by a cubic parabola, and the divergent part is calculated using the method of characteristics (MOC). Figure 1 shows a representative example of Bluebell nozzle surface geometry. The x axis coincides with the nozzle axis of symmetry.

A Bluebell nozzle has a sinusoidal lip line edge, i.e. the nozzle edge distance from the nozzle throat, $x = x_e$, that changes sinusoidally vs azimuth angle φ, with variation in amplitude ε. The cross sections of the nozzle divergent part also are limited by sinusoidal curves vs angle φ, so that the variation amplitude in surface $r(x, \varphi)$, increases along a nozzle centerline from zero at the cross section $x = x_0$ downstream a throat to the maximum value at the exit $\delta = \delta_0(x - x_0)$. The cross section, x_o, is chosen to have an axial flow velocity slightly exceeding the local sound velocity (M_x=1.01 to 1.03, for details see below the next part). Finally, the lateral surface equation of a Bluebell nozzle can be written as:

$$0 \leq x \leq x_e(\varphi), \tag{1.1$_a$}$$

$$r(x, \varphi) = R_n(x)[1 + \delta\cos(n_c\varphi)], \tag{1.1$_b$}$$

$$x_e(\varphi) = x_e^o[1 + \varepsilon\cos(n_p\varphi)], \tag{1.1$_c$}$$

where n_p, n_c are variation frequency of longitudinal lip line change and cross section correspondingly. These values are assumed to be even numbers. For simplification of description, these variations are denoted as "chevrons" (or "petals") and "corrugations".

We require the same mass flow rate for Bluebell and baseline nozzles in each cross section. Thus at each nozzle cross section, Bluebell nozzles have the same cross section area, $S_n(x)$, as the reference baseline nozzle, $S_0(x)$. From this equality in cross section area, the coordinates $R_n(x)$ are derived from equation 1.1a through 1.1c. Bluebell nozzle cross section area $S_n(x)$ is calculated by the simple formula and function $R_n(x)$ explicitly expressed by baseline radius $R_o(x)$:

$$S_n(x) = \frac{1}{2}\int_0^{2\pi} r^2(x, \varphi)d\varphi = \pi R_n^2(x)(1 + \frac{\delta^2}{2}), \tag{1.2$_a$}$$

$$R_n(x) = R_o(x)/\sqrt{(1 + \frac{\delta^2}{2})}, \tag{1.2$_b$}$$

Here it is assumed that $R_o(x) = R_o(x_e^o)$ for $x \geq x_e^o$, where $x \geq x_e^o$ is a baseline round nozzle edge.

A divergent part lateral surface area and a lip line length in general can only be calculated numerically for the table data $R_o(x)$. For some particular cases these values can be defined analytically. For example, a lip line length of a Bluebell nozzle without petals ($\varepsilon = 0$) is expressed by elliptical functions and, additionally, if it is assumed that $\delta = 1$, the appropriate integral is defined by the elementary functions:

$$L_n = \int_0^{2\pi} f(\varphi)d\varphi = 2 + \frac{2}{n\sqrt{n^2 - 1}}(\ln(n + \sqrt{n^2 - 1}),$$

$$f(\varphi) = \sqrt{r^2(x,\varphi) + r'^2(x,\varphi)},\ x = x_e^o \qquad (1.3)$$

A lateral surface area S_n can be defined analytically for conical nozzles with divergent angle α and we have:

$$S_n = \frac{1}{\cos\alpha}\int_0^{2\pi}\int_{x_*}^{x_e(\varphi)} r(x,\varphi)dxd\varphi \qquad (1.4)$$

where $r(x,\varphi)$ is given by (1.1) and $R(x) = 1+\tan\alpha\cdot(x-x_*)$. The integral (1.4) can be expressed by elementary functions. We write this formula for a nozzle with petals without corrugations ($\delta_o = 0$):

$$S_n = \frac{\pi x_e^o}{\cos\alpha}(2 + x_e^o\tan\alpha + \frac{1}{2}\tan\alpha x_e^o\varepsilon^2) \qquad (1.5)$$

Note that the cross section "equivalent" radius of a Bluebell nozzle $R_n(x)$ is independent of frequency n_c, the lip line length increases with both n_p and n_c, as well as the lateral surface area. For small values of ε and δ, this increase is small.

Some results of numerical integration of (1.1), (1.3) and (1.4) for Bluebell nozzles with $M_e = 1.5$ is illustrated in Figure 2a and 2b. Apparently, these lip line length ratios,L_n/L_0, are more dependent on δ than lateral area ratios. The lateral area ratios are close to one for small values of δ. This is very important for practical applications, to minimize wall friction effects.

Another Bluebell nozzle embodiment is based on the MOC designed round nozzle with extended cylindrical pipe ($r = R_o(x_e^o)$ at $x \geq x_e^o$). Such design provides more uniform pressure distribution at the lip line edge and this reduces the barrel shock intensity in the jet exhaust. In particular, a nozzle with petals, just without corrugations ($\delta_o = 0$), is a shock free nozzle. In this case such a design has less thrust than the corresponding first embodiment. Two embodiments are shown in Figure 3a and 3b: a)-1st embodiment of 8-petal Bluebell nozzle, b)-2nd embodiment of 4-petal Bluebell nozzle.

2. THE THEORY, NUMERICAL METHODS.

2.1. The theoretical approach. The general purpose of the theoretical approach is to define the optimum conditions which provide minimum Bluebell nozzle thrust loss by comparison with the baseline convergent divergent design, or conical nozzles. To achieve an optimal nozzle design, the solution would reguire multiple computations of a 3-D supersonic flow region. For practical applications, unit Reynolds numbers Re are very high $10^6 - 10^8$. So that the boundary layer at the wall is turbulent and makes up a small portion (~ 1-3%) of the cross section size and even less to some extent effects the longitudinal nozzle size. For example, in accordance with [4], the ratio of the local boundary layer thickness,δ^*, to the distance, x, along a flat plate is dependent on the local Reynolds number, Re_x, as given by the relationship:

$$\delta^*/x = 0.02\cdot Re_x^{-1/7} \qquad (1.6a)$$

The local wall skin friction coefficient $c_f = \tau_w/(\frac{1}{2}\rho_\infty {U_\infty}^2)$ is given by

$$c_f = 0.0263\cdot Re_x^{-1/7}/(1 + \frac{k-1}{4}M_\infty^2)^{5/7} \qquad (1.6b)$$

In such a situation it is inefficient to use numerical solution based on the full unsteady Navier-Stokes equations. Our approach is based on the "viscous-inviscid interaction" [4]. We used the Euler approximation for definition of the "external" inviscid flow outside a thin boundary layer whose thickness is defined by equation 1.6a with friction along the nozzle wall defined by equation 1.6b. The Euler calculations were repeated for each new nozzle shape ($r = R_1$) after accounting for the boundary layer thickness (δ^*), i.e. $R_1(x,\varphi) = R(x,\varphi) - \delta^*(x,\varphi)$. The new computed "external" inviscid flow again was used for definition of a new boundary layer thickness. In each iteration, of course, the boundary layer is computed at the original nozzle surface $r = R(x,\varphi)$. Usually, the results were closed after several iterations, between 3 and 4.

Subsonic and transonic flow numerical simulation in the convergent nozzle part was conducted in the interval $0 \leq x \leq x_o$ by an implicit upwind 2nd order numerical scheme (ENO-version) for solution of the full unsteady Navier-Stokes equations, as incorporated in the CRAFT code of CRAFT-Tech (see Dash [5]). This code was originally developed by Molvik and Merkle [6]. The algorithm's capability, along with several modifications with different applications, are described in a set Dash's et al. papers. Thus we omit its description completely. We modified this code, so that in some time intervals of the Euler stage computation, we could adapt Spalding's code [7, 8] for boundary layer computation. With Spalding's code we made a correction of the nozzle boundary location and then continued computation by the CRAFT code. Such procedure is repeated until two consequent iterations differ less than a given small value. Note also, that in most of our computations, the problem is two-dimensional, since we are able to assume that in this interval the nozzle is axisymmetric. Recall that the cross section, x_o, is chosen to have an axial flow velocity slightly exceeding the local sound velocity ($M_x = 1.01 - 1.03$). Several variants of completely 3D problems were computed by this method using CRAFT-Spalding combination code. We used that only for comparison and examination of the main results obtained by 2D and 3D marching schemes. The grid at the Bluebell nozzle surface is shown in Figure 1. It is based upon the cylindrical coordinate system, which transforms to the normalized (ξ,η,φ) system, so that in the x and r directions the computational region becomes a unit square in ξ,η variables $(0 \leq \xi \leq 1, 0 \leq \eta \leq 1)$.

2.2. Krayko-Godunov numerical scheme.

Numerical simulation of supersonic flow in the divergent nozzle part and exhaust jet was conducted by Kryko-Godunov explicit 1st order numerical scheme (K-G-code) [9, 10].

Consider a cylindrical coordinate system (x, r, φ) with components of a velocity vector **q** on these axes of (u,v,w), and let q be a modulus of a velocity vector **q**, p is a pressure, ρ is a density. All variables are nondimensional. Linear sizes are related to a throat radius r_*, velocities-to a sound velocity c_* in the nozzle critical section (throat), density by the critical density ρ_*, pressure by $\rho_* c_*^2$. The gas is assumed perfect with constant specific heat coeficients c_p and c_v, so that specific heat ratio $k = \frac{c_p}{c_v}$ is constant. The Euler equation is written in the form of the integral conservation laws:

$$\frac{d}{dx}\int\int_{\Sigma} \mathbf{a}\; dr d\varphi = \oint_{L} [(\mathbf{c} - \mathbf{a}\; \varsigma^{\varphi})dr - (\mathbf{b} - \mathbf{a}\; \varsigma^{\mathbf{r}})d\varphi] +$$

$$+\int\int_{\Sigma} \mathbf{f}\; dr d\varphi \qquad (1.7)$$

$$\mathbf{a} = (\,\rho u \quad p + \rho u^2 \quad \rho u v \quad \rho u w\,)$$

$$\mathbf{b} = (\,\rho v \quad \rho u v \quad p + \rho v^2 \quad \rho v w\,)$$

$$r\mathbf{c} = (\,\rho w \quad \rho u w \quad \rho v w \quad p + \rho w^2\,)$$

$$\mathbf{f} = -\frac{\rho}{r}(\,v \quad uv \quad v^2 - w^2 \quad 2uv\,) \qquad (1.7a)$$

$$\frac{2k}{k-1}\frac{p}{\rho} + q^2 = \frac{k+1}{k-1} \qquad (1.8)$$

where vectors **a**,**b**,**c** and **f** are the conservation variables written by the rows instead of by the usual columns; L is some reserved contour, which limits the area Σ in an arbitrary cross section, $\varsigma = \frac{\mathbf{dn}}{dx}$, where **dn** is a projection of displacement L to an outward normal. Vectors ς and **dn** are perpendicular to $x-$axis in each point of a contour L. They are completely defined by their projections ς^r and ς^{φ} to the r and φ axes. The equation (1.8) is the condition for a total enthalpy conservation ,H_o, which along with equation (1.7), completely defines the system.

Some elements of the applied 3D fixed grid are illustrated in Figures 4a and 4b. In a plane r,φ the regions between several boundaries $R_2(\varphi)$, $R_1(\varphi)$, ..$R(\varphi)$ in the r-direction and between two symmetry planes $\varphi = 0$,$\varphi = \pi/n_c$ in φ-direction are split by K radial straight lines φ =const and J lines ξ =const. The η lines contain straight intervals between appropriate splitting points of neighboring radial lines. A splitting in the φ-direction (h_{φ}) is chosen uniform, and in r-direction (h_r) as a geometric progression with a denominator that is defined by equality of the neighbor cell sizes at both sides of each boundary. This provides uniform accuracy for numerical results near boundaries, which can represent shock waves, slip shocks, or usual streamline surfaces. The step size, h_r, increases near the axis of symmetry.

The known flow values at cross section, $x = x_i$, will define those in the following section $x_{i+1} = x_i + h_x$. Two neighbor six-side grid cells are shown in Figure 4b. For each cell (as control volume) we write the conservation laws (1.7) using the explicit 1st order finite-differential scheme, which includes the conservation variable values at the lateral cell sides:

$$\mathbf{Q}^{j-\frac{1}{2},k-\frac{1}{2}} = \mathbf{Q}_{j-\frac{1}{2},k-\frac{1}{2}} + \mathbf{E}_{j,k-\frac{1}{2}} - \mathbf{E}_{j-1,k-\frac{1}{2}} -$$

$$\mathbf{G}_{j-\frac{1}{2},k} + \mathbf{G}_{j-\frac{1}{2},k-1} + \frac{h_x}{2}(\mathbf{F}_{j-\frac{1}{2},k-\frac{1}{2}} + \mathbf{F}^{j-\frac{1}{2},k-\frac{1}{2}}) \quad (1.9)$$

$$\mathbf{Q} = \mathbf{a}h_r,\; \mathbf{E} = (\mathbf{A}\Delta_1 - \mathbf{B}h_x + \mathbf{C}\Delta_2\frac{h_x}{h_{\phi}})$$

$$\mathbf{G} = \mathbf{C}\frac{h_x h_c}{h_{\phi}}, \qquad \mathbf{F} = \mathbf{f}h_r \qquad (1.10)$$

Here the subscripted indicies correspond to the known values (in a plane x_i) and superscripted indicies to the determined values (in a plane x_{i+1}). Whole indicies j, k correspond to cell interface, non-whole indecies $j-\frac{1}{2}$, $k-\frac{1}{2}$ to a cell center. Value Δ_1 represents an average increment of side radial coordinates (super or under) from i to $i+1$ cross sections, and Δ_2 represents an average inclination of these sides. The vectors are designated by big letters **A**,**B**,**C** and they correspond to the similar small conservative values **a**,**b**,**c** for cell centers of the cross sections x_i,x_{i+1}. In Figure 4b all cell tops are assigned by letters, where even subscript numbers at the cell tops are for the upper cell side; odd subscript numbers are for lower cell-side. The stars in the cell centers depict points at which flow parameters are known and determined for each cell.

Big values are used to determine the elementary solutions by considering the similar two-dimensional steady problem of two uniform unlimited interacting supersonic flows. Depending on the relational flow direction, the pressure and density ratio from different locations and combinations of the shock waves, uniform flow regions, slip shocks and rarefaction waves were obtained. We can consider such an interaction problem by assuming that flows in the neighboring grid cells are uniform at each cell interface. There are five main possible mutual locations of the cell interface and similar flow regions ([13]). Determined values correspond to the similar solution in one of the regions. These solutions require iterations. Linear (acoustics) approximation (Riemann solver) allows us to avoid these iterations. However, such an approach doesn't provide the necessary accuracy of numerical solution, and in some cases requires a low Courant number. Usually, for boundary cells we have to apply the nonlinear approach; especially for lip shocks. Of course, extraction of the barrel shock waves, lip shocks, and bow shocks for flight simulation always require a nonlinear approach.

We omit all finite relationships of these similar solutions (see [10] for details). Note only that for this explicit scheme a step in the x direction, h_x, has satisfied the stability condition $h_x = Cu \cdot H_r H_\phi / (H_r + H_\phi)$, where Cu is Courant number, $H_r = \min(H_1, H_2)$, H_1 is a distance in x direction, where a corresponding wave formed by an interaction at the r_{j+1} cell top (M_2) reaches the neighbor cell top $r^j(M_3)$, and H_2 is a similar distance for $r_j(M_1)$ and $r^{j+1}(M_4)$. Similarly the value H_ϕ is defined.

The algorithm was tested against the exact solution of the following problems: 1D flow from a point source, 2D Prandtl-Meyer rarefaction flow, a flow around a wedge and 2D shock wave reflection from a plate. Comparison was also made to a similar solution for a flow around a cone. For each case sensivity to grid variation was studied and the integral conservation law for flow in each cross section was examined. The different tests show that the algorithm achieves high resolution and is very fast and economical, especially with 2D flow simulation. For example, a computation by 2D "K-G" code with 100 cells in a cross section leads to an error less than ~ 0.1%. For the jet nozzle flow field and nozzle plume extending to 50 jet radii, the computation requires only about 60 sec. on an INDIGO III computer workstation.

The same tests were applied to the 3D flow. Note that 1D flow from a point source in a cylindrical coordinate system is a 3D problem, if a point source origin is not located in the x-axis of this system. Of course, this code required more time for the computation to reach the given accuracy of less than ~ 0.1%. The grid J×K=60 ×10 provides an accuracy of ~ 0.3 to 0.5% for pressure distribution along the nozzle wall. These estimations are guaranteed for a Bluebell nozzle with $n_p = n_c = 4$ and 8, and $\varepsilon \leq 0.3$, $\delta_o \leq 0.2$.

An example of such test results is shown in Figures 5a,5b and 5c. Figure 5a illustrates Mach contours computed by 2D "K-G" code of a supersonic flow with $M_\infty = 3$ into a wedge-shaped inlet with angle $\alpha = 5^o$. Here only the upper half flow from the symmetry plane to the wall is shown. The code used 100 cells in each cross section with uniform step h_y. The oblique shock wave at the wedge repeatedly reflects from the symmetry plane and from the wall. The reflected shock waves are inclined at the angle β_m, the reflection coordinates and all constant flow parameters at the shock interface are calculated by the exact relationships on oblique shock waves and by simple geometric relationships. This is reached by solving the implicit equation:

$$\tan\alpha = \frac{f(\beta_m)/\tan\beta_m}{1 - f(\beta_m)}, \quad f(\beta) = \frac{2}{k+1}(\sin^2\beta - M^{-2})$$

with the help of the Newton iterations relative to the shock wave angle β_m. Pressure distributions computed by the exact method and the 2D K-G code are shown in Figure 5b along the plane of symmetry and in Figure 5c along the wall. The error of the numerical scheme increases between 0.5 and 1% after 1 to 4 reflections from both walls. The accuracy of the numerical solution increases with increasing flow Mach number, M_∞, or the wedge angle α.

2.3 The boundary layer Spalding's numerical method. This algorithm is based on a six-point 2nd order, implicit finite-difference scheme for the 2D steady compressible boundary layer numerical solution. This method and algorithm is described by S. Patankar and D. Spalding in [10, 11]. The energy and momentum equations are cast in terms of the Mises variables (x, ψ), where ψ is a streamline function. This SPALD-2 code is very fast and convenient for nozzle-jet numerical simulations, and for examination of different turbulence models. We used this code for 2D problems and modified it for 3D boundary layer problems. The subsonic and transonic flow is defined by the sequential iterations with external flow as we described above in item **1.2.1**. In the supersonic region we use this code as a subroutine in combination with 2D and 3D "K-G" codes. The appropriate iterations were conducted in each cross section x =const and the defined "equivalent" nozzle boundary. For a supersonic flow into a Bluebell nozzle, where $n_c = n_p = n$, there are 2n planes of symmetry. Therefore it is sufficient to compute only between two planes in the interval $(0 \leq \varphi \leq \pi/n)$. In each of these planes a boundary layer is two-dimensional, if one ignors second derivatives in the φ direction. Assuming that the 3D boundary layer thickness is $\delta^*(x, \varphi)$ and the friction at the wall is $\tau_w(x, \varphi)$, one can be approximate these by the function

$$g(x, \varphi) = \frac{g_o(x) + g_K(x)}{2} \cos n\varphi + \frac{g_o(x) - g_K(x)}{2}$$

where subscript indicies o and K correspond to their values in $\varphi = 0$ and $\varphi = \pi/n$ planes of symmetry. In the above relation g is either δ^* or τ_w. Comparison with the full NSE simulation results shows that such an approximation is effective for $n \geq 4$, $\varepsilon \leq 0.3$, $\delta_o \leq 0.3-0.4$, and when the nozzle is operated nearly fully pressure balanced (i.e. $p_e \sim p_\infty$) A similar approximation has been applied earlier for 3D supersonic flows around blunt bodies.

The turbulent boundary layer theoretical model [7, 8] is based on the Prandtl mixing-length hypothesis, a one-dimensional representative flow near a wall

(Couette-flow) and the van Driest [11] hypothesis, which introduces an "effective" viscosity near a wall as:

$$\mu_{eff} = \mu + \rho K^2 y^2 [1 - \exp\{-y\sqrt{\tau\rho}/(\mu A_+)\}]^2 |\partial u/\partial y|$$

where A_+, K are constants, y is the normal direction to the wall, μ is a laminar viscosity, $\rho K^2 y^2 |\partial u/\partial y|$ is a turbulence viscosity, and the latter is "damped" near the wall in an exponential fashion.

2.4 Thrust calculation. In accordance with traditional thrust definition, introduce P and the corresponding nondimensional value T as:

$$P = \int_{\Sigma_e} (\rho_e {u_e}^2 + p_e) d\Sigma - p_\infty \Sigma_e, \quad T = \frac{P}{p_o \Sigma_*} \qquad (1.11)$$

where subscript indices e, ∞, o and $*$ are assigned to the nozzle exit cross section, ambient, total and critical (in a throat) parameters correspondingly. Σ_* is a throat area. The integrand expression in (1.11) is called an impulse function [13]. Such a definition is introduced for rocket motors, but it doesn't take into account vehicle drag, and assumes the same shape of the external and internal vehicle surfaces. Therefore it only approximates the real vehicle net thrust. Nevertheless we will use this definition for an estimation of the nozzle shape variation influence on the thrust. The ideal thrust of a nozzle is determined from the quasi-one-dimensional approximations assuming an isentropic perfect gas. These are simple formulae, available in many textbooks, for example, in [13]. Let us define, $T_{id}(k, n_{eo})$, as the thrust of the ideal nozzle, and ΔT_{id} is the thrust augmentation from the supersonic (divergent) part of such a nozzle. These values are calculated with the base formulae (4.34), (4.35) in [13] and are completely defined by specific heat ratio k and pressure ratio $NPR = p_o/p_\infty$. We will define the thrust T and its augmentation ΔT directly by integration of the impulse function at the inlet cross section I_o, and the difference between pressure and friction along the nozzle wall. The integral of the impulse function at the nozzle exit, taking into account the boundary layer, allows us to estimate the integral error of the applied numerical scheme. Thus the thrust for a single design is calculated using the above nondimensional variables as:

$$T = B(I_o + I_1) - \frac{p_\infty}{p_o} \cdot \frac{\Sigma_e}{\Sigma_*}, \quad B = \frac{k}{\pi}\left(\frac{2}{k+1}\right)^{\frac{k}{k-1}}$$

where

$$I_o = \int_0^{x(\varphi)} \int_{r_o}^{r_e} \int_0^{2\pi} p(1 - \frac{k}{2} {M_w}^2 c_f \sin\alpha) r\, dx\, dr\, d\varphi$$

$$I_1 = I(x_o) = \int_0^{r_o} \int_0^{2\pi} (p + \rho u^2) r\, dr\, d\varphi$$

and

$$\Delta T = T - T_* \qquad (1.12)$$

where T_* is the thrust of a convergent nozzle part.

2.5 Numerical simulation results. Using the above approach and numerical schemes, we conducted simulations of the internal flow in the Bluebell nozzles and the exhaust jet. These simulations included a wide diversity of nozzle geometries, in particular, variation of the petal and corrugation coefficients ε, δ_o, their frequencies n_p and n_c, exit Mach numbers M_e, and baseline nozzle variation. (i.e. conical and optimal axisymmetric nozzles). All nozzles were designed using the same convergent nozzle geometry.

We concentrated on a baseline nozzle for shock free flow with $M_e = 1.5$. We obtained acoustic data for this nozzle. Figure 6 illustrates Mach contours for the four-petal nozzle with $\varepsilon = 0.7$ and $\delta_o = 0.2$. Here there are two meridional planes of flow symmetry- $\varphi = 0^o$ and 45^o. They are limited by the axis of symmetry, nozzle boundary and inviscid jet boundary from the nozzle throat at $x = 0$, to the end of the fourth barrel at $x = 10$. Additional pictures of five cross sections of Mach contours are also presented. They help to see the jet shape and flow structure. These cross sections are located at the nozzle throat ($x = 0$), two at internal nozzle cross sections, x_2=1 and x_3=2.5, close to the nozzle exit, x_4=4 and at the end of the computed interval x_5=10.

Apparently, the round shape deforms to a round-rectangular shape and later downstream takes a shape similar to petals or a flower: a round part transforms to rectangular, and rectangular to almost triangular. The petals become sharper, which promotes more intensive whirlwind formation and more effective mixing with ambient air. This also confirms the observation of the pressure contours and velocity maps.

The formation of the whirlwind inside corrugations is distinctly illustrated in Figure 7. Here Mach contours are shown for an eight-petal nozzle with $\varepsilon = 0.35$, $\delta_o = 0.2$, $n_p = n_c = 8$. The favorable conditions for whirlwind formation appear at once after the throat.

Figure 8 shows development of cross section pressure contours, and jet shape in the planes of symmetry for a nozzle pressure ratio NPR=17. For underexpended jets such mixing intensification increases, which is expected. The flow through the "gaps" between petals penetrates into ambient air forming shapes like that of an ear and at the nozzle exit, $x_4 = 4$ the cross section has a butterfly shape with whirlwind flow into its wings. The closed pressure contours show existence of vortical flow. Near the end of the first barrel, the cross section transforms to an X-shape.

More detailed pictures of Mach contours for this case are shown in Figures 9a and 9b, where 2D plots are presented for two planes of symmetry $\varphi = 0$ and $\varphi = 45^0$. A velocity map in the cross section, $x_4 = 4$, for the case shown in Figure 6 is illustrated in Figure 10. The whirlwind flow is observed very well; gas follows from the nozzle interior to a concave part of the wall surface.

Unfortunately, we could not simulate 3D mixing layers effectively and observe formation, development and destabilization of the vorticities starting from the nozzle exit and moving downstream in the jet exhaust. For this we need to use a large-eddy simulation (LES) approach with correspondent codes, however, even for 2D problems such computational work is very expensive.

The main numerical results concerning thrust optimization are represented in Figure 11, which show the ratio of the Bluebell nozzle-first embodiment relative to the baseline nozzle thrust, T_n/T_o, vs nozzle geometric parameters. All comparisons are performed for exhaust Mach number $M_e = 1.5$. There are several curves that illustrate the contribution of different nozzle geometric factors to the thrust: viscous effects, petals and corrugations. The parametric intervals used are limited by restrictions in the numerical scheme following from the condition $M_x > 1$. The dependence of the thrust on the corrugation coefficient and frequency is found to be more significant than from petal values. The influence of the petal length (ε) is nonmonotonic; for small values $\delta_o < 0.025$ the thrust reduces with ε increasing, but increases with ε, when $\delta_o > 0.025$ and $\varepsilon \leq \varepsilon_m$. These curves represent the maximum values achieved by the Bluebell nozzle geometry. Several factors influence the behavior of these curves. The first occurs from increase of the nozzle length with corresponding “effective“ Mach number increase at the exit. Of course, for the case $\varepsilon > 0$ the term “exit“ is a conditional understanding and Mach number can change significantly along the exit lip line. On the one hand a lateral flow reduces a pressure at the wall, but on the other hand it reduces the “effective“ boundary layer thickness δ^*. The flow expands into the nozzle's channels and this creates additional thrust by hydrodynamic pressure on the “lateral sides“ of such channels. This conclusion is confirmed by Figure 12, where pressure distributions are shown along the wall in the several cross sections for cases described above.

Another dependence observed for the Blubell nozzle-second embodiment is presented in Figure 13. The thrust ratios are similar to those observed for the previous case. There is some thrust loss from the friction of the gas flow from the almost horizontal additional sheet with petals. However, this thrust loss is insignificant and does not exceeded $1 - 2\%$. This is much less than thrust losses encountered for nozzles described in [2, 13] that suppress noise.

The general conclusion obtained from the numerical simulation is that there is an optimum set of geometric parameters, which provide a maximum thrust exceeding the usual round nozzle thrust. The influence of such nozzle shape variation on jet noise is examined below.

3. ACOUSTIC DATA.

3.1. Experimental approach. The Bluebell nozzle design takes into account all theoretical and numerical understanding discussed above. Nine different nozzles were made including the baseline round nozzle. The list of these nozzles assigned by numbers #1 thru #9 is represented in Table 1, along with their geometric parameters $n = n_p = n_c, \varepsilon, \delta_o$. In Table 1, nozzle #7 is the round convergent baseline nozzle and nozzle #9 is the round convergent-divergent baseline nozzle. Four of them are shown in Figure 14.

Table 1

N	1	2	3	4	5	6	7	8	9
n	8	8	8	8	4	4	0	8	0
ε	0.23	0.23	0.38	0.15	0.45	0.45	0	0.23	0
δ_o	0.20	0.00	0.00	0.00	0.20	0.00	0	0.10	0

All nozzles have a throat radius r_*=0.6373in. The round nozzle has the exit radius r_e^o= 0.6943in. The Bluebell nozzles have exit radii defined by equation (1.2b). The length of the convergent part of all nozzles is x_*= 2.053in, and the entire length of the baseline round nozzle is x_e^o=4.25in. All Bluebell nozzles are made on the base of the second embodiment, with use of the additional sheets. Their lengths are varied from the baseline nozzle by an additional 1.0 to 1.1 inches depending on the geometrical parameters selected for the nozzle.

The experiments were conducted in the small Anechoic Jet Noise Facility (SAJF) at the NASA Langley Research Center. Figure 15 shows part of this facility with Bluebell nozzle #1. The interior dimensions of the facility within the wedge tips are 10x13x8ft high. The anechoic treatment absorbs at least 99% of incident sound at frequencies greater than 150Hz. The air system provides a supply of continuous dry unheated or electrically heated air at mass flow rates of 2lb/s and maximum stagnation pressure of 150 psia. Nozzle pressure ratios ($NPR - p_o/p_\infty$) are controled electronically within 0.3%. The nozzles are fastened at the end of a 2.500-in straight diameter pipe section that extends 24in. The upstream end of this pipe is connected with a contoured transition section to a 3“ diameter pipe section which contains a flow straightner. Air is supplied through this pipe system to the nozzle, and can reach temperatures of 1000^oF.

Three 1/4in-dia. microphones were located along the wall. The sketch of the location of the microphones and nozzle-jet system is shown in Figure 16. All dimensional values are presented for microphone locations in the figure. The data from these microphones was low passed filtered at 100kHz, amplified and digitized before being sent to the computer for storage and analysis.

1.3.2. Experimental results. All nozzles shown in Table 1 were tested at both supersonic and subsonic conditions. In the supersonic regime the nozzles were operated slightly underexpanded at the nozzle pressure ratio NPR=4.0 and jet total temperature $T_j = 350^oF$. This corresponds to a fully expanded jet Mach number of 1.56 with corresponding exit velocity of 1740 ft./sec. All nozzles, except convergent nozzle 7, were designed for a fully expanded Mach number $M_e = 1.5$. The underexpanded condition was selected because it was expected that the nozzles with corrugations would reduce noise more effectively at this condition. In the subsonic regime the nozzles were operated at the nozzle pressure ratio NPR=1.27 and jet total temperature of 538^oF This corresponds to an exhaust Mach number $M_e = 0.6$ with corresponding exit velocity 900 ft./sec. At either supersonic or subsonic nozzle operating conditions the nozzles were sized to operate at the same ideal thrust.

Due to the small size of the nozzles of Table 1, it is not possible to display acoustic data in terms of the percieved noise level (PNL) metric. Instead we shall show comparative results in terms of the measured overall sound pressure level and then show comparative narrow band spectra of those nozzles of most interest.

Figures 17a and 17b show the overall sound pressure level results for all nozzles. Figure 17a compares results at the supersonic condition and Figure 17b those at the subsonic condition. In the supersonic regime the overall levels are shown as differences relative to that measured from the baseline convergent-divergent nozzle with design exhaust Mach number of 1.5. In the subsonic regime the reference nozzle is the baseline convergent nozzle. In both the supersonic and subsonic regimes, the reference nozzles produced maximum sound radiation at the angle $\Psi = 145^o$. Figure 17a shows that all nozzle concepts produced varying levels of noise reduction at the peak radiation angle, and even at $\Psi = 91.1^o$. The noise reduction at $\Psi = 125.7^o$ was the least, even indicating levels above the baseline nozzle. In all cases those nozzles with corrugations displayed the best acoustic performance (i.e. nozzles 1,5 and 8). Also increasing the nozzle perimeter leads to improved levels of noise reduction.

Figure 17b indicates that most nozzle configurations actually produced more noise than the baseline convergent nozzle. The only one showing some promise is nozzle 1. The results shown in Figure 17a and 17b are not surprising. In the supersonic regime, noise is heavily driven by Mach wave emission, where it is generally a good practice to select a suppression concept that enhances mixing. However, we now have observed the following anomalous behavior, nozzle 1 works well in both flow regimes. Thus it is important that we show details of the narrow band spectra for this nozzle to see where the noise reduction occurs.

Figures 18a, 18b, and 18c show respectively narrow band spectra for angles $\Psi = 91.1^o, 125.7^o$, and 145^o to the nozzle inlet. These spectra are acquired at the supersonic condition. All spectra were computed from digitized time records using a 2K FFT, which provides a spectral resolution of 100 Hz. From Figure 18a one clearly can observe the presence of screech and broadband shock noise in the reference nozzle 9. This is expected due to operation at the slightly underexpanded condition. Note, however, that Bluebell nozzle 1 has significantly reduced shock noise, but it is difficult to determine if the high frequency range contains shock noise above 20 kHz. for this nozzle. The Figure 18c spectrum shows that the noise reduction achieved in the peak radiation direction occurs over the entire spectral range.

Figures 19a and 19b show respectively narrow band spectra for angles $\Psi = 91.1^o$, 125.7^o, and 145^o to the nozzle inlet axis. These spectra are acquired at the subsonic condition, and comparison is made to the convergent-divergent nozzle used in the previous figure, since it is nearly equivalent to that of the convergent nozzle. Even though Figure 17b shows a reduction in OASPL for Bluebell nozzle 1 in the subsonic regime, these spectra indicate that noise reduction would not be evident in the PNL metric. This is due to the cross-over in the spectra beyond 5kHz. Thus the anomalous behavior of Bluebell nozzle 1 is now explained, this nozzle enhances mixing in the subsonic range but actually increases noise in the PNL metric.

II. DISCUSSION AND CONCLUSIONS

In this paper we have examined both the thrust and noise performance of several round axisymmetric nozzles designed with chevrons and corrugations, and have made comparisons to reference baseline convergent- divergent $M_e = 1.5$ and convergent nozzles. All nozzles with chevrons and corrugations were designed as convergent-divergent nozzles with exhaust Mach number $M_e = 1.5$. The thrust calculations were performed using the Krayko-Godunov numerical scheme (Euler based) both with and without boundary layer correction. Additional thrust calculations were performed using a full Navier-Stokes code with k-ε turbulence model for select cases.

The thrust calculations for the supersonic regime demonstrated that Bluebell nozzle 5, with $\delta_0 = 0.2$ and $\varepsilon = 0.45$ (i.e. curve 2 in Figure 11), actually has augmented thrust in the range of 1%. The noise data for this nozzle (i.e. Figure 17a) exhibits a reduction of noise of nearly 4 dB. The thrust calculations also indicated that even better aeroperformance could be obtained at greater values of the corrugation amplitude δ_0 and also with increase in nozzle perimeter, as reflected through the parameter ε. The noise results also showed that increased suppression is obtained with increasing values of δ_0 and ε. Unfortunately, we have not constructed such a model nozzle, nor have we as yet predicted or measured the turbulent flow field to further confirm these results. This is being addressed at this time. The thrust calculations also revealed that standard methods usually applied to account for boundary layer thickness with an Euler solver provide misleading results. The Navier-Stokes simulations have shown better agreement with the Euler code without boundary layer correction.

The subsonic acoustic results were disappointing, yet not entirely unexpected. They demonstrate what we have known for a long time. Noise reduction is very difficult to achieve at low exhaust velocities. At high velocities noise reduction is simply achieved through enhanced mixing, although, in general, it comes as a trade-off with aeroperformance. Thus the Bluebell nozzle without ejector is an exception. With an ejector one expects even better aeroperformance and noise suppression from the Bluebell nozzle, and it may even be possible to achieve this in the subsonic regime. As stated in the introduction, one needs to investigate the turbulent acoustic source to properly optimize the nozzle geometry, particularly in the subsonic regime.

III. ACKNOWLEDGEMENTS

We would like to acknowledge the fellowship support of the National Research Council at NASA Langley Research Center. We would like to acknowledge the Jet Noise Team support, especially, M. Ponton and D. Saliga for the active help in the treatment of the experimental data. We would like to thank Dr. J.C. Hardin for his attention, interest to our research, review and useful suggestions.

IV. REFERENCES.

1. Seiner, J.M., and Gilinsky, M.M., 1993, A Bluebell Nozzle for Improving the Mixing of Exhaust Jets with Ambient Air, Invention Disclosure, NASA Case No. LARC-15215-1.

2. Seiner, J.M., and Krejsa E.A., 1989, Supersonic Jet Noise and the High Speed Civil transport, AIAA Paper 89-2358, AIAA/ASME/SAE/ASEE 25 Joint Propultion conference, July 10-12, 1989/Monteray, CA.

3. Presz, W.M., Jr., 1991, Mixer/Ejector Noise Suppressors, AIAA Paper 91-2243, AIAA/SAE/ASME 27th Joint Propultion Confference, June 24-26, 1991/ Sacramento, CA.

4. Loitzansky, L.G., 1973, Mechanics of Liquid and Gas, Moscow: Physico- Mathematical Literature, 847p.

5. Dash, S.M. et al., 1993, Progress in the Unsteady Simulation of Jet Flowfield, AIAA/SAE/ASME/ ASEE 29th Joint Propulsion Conf. and Exh., Jun. 28-30, 1993, Mont., CA.

6. Molvik, G.A. and Merkle, C.L. 1989, A Set of Strongly Coupled, Upwind Algorithms for Computing Flows in Chemical Nonequilibrium, AIAA Paper 89-0199, 27th Aerospace Sciences Meeting, Jan. 9-12.

7. Patankar, S.V. and Spalding, D.B., 1967, A Finite-Difference Procedure for Solving the Equation of the Two-Dimensional Boundary Layer, Int. Journ. Heat and Mass Transfer, vol.2, No 10, 1389-1412.

8. Patankar, S.V., Spalding D.B., 1968, Heat and Mass Transfer in Boundary Layers, C.R.C. Press: Cleveland, 1968, 138p.

9. Ivanov, M.Ya., Krayko, A.N. et al., 1973, Thorough Computational Method for Two and Three-Dimensional Supersonic Flows, Journal Vychislitel'noi Math. i Math. Phisiki, v.12, No 2, pp. 441-463.

10. Godunov, S.K. et al., 1976, Numerical Solution of Multidimensional Problems of Gas Dynamics, Moscow: Nauka, 1976, 400p.

11. Van Driest, E.R., 1956, On Turbulent Flow near a Wall, J.Aeronaut. Sci., 23, p.1007.

12. Shapiro A.H., 1953, The Dynamics and Thermodynamics of Compressible Fluid Flow, v.1, The Ronald Press Co., New York.

13. Seiner J.M., 1984, Advances In High Speed Jet Aeroacoustics, AIAA Paper 84-2275, AIAA/NASA 9th Aeroacoustics Conference, Oct. 15-17, 1984/Williamsburg, VA.

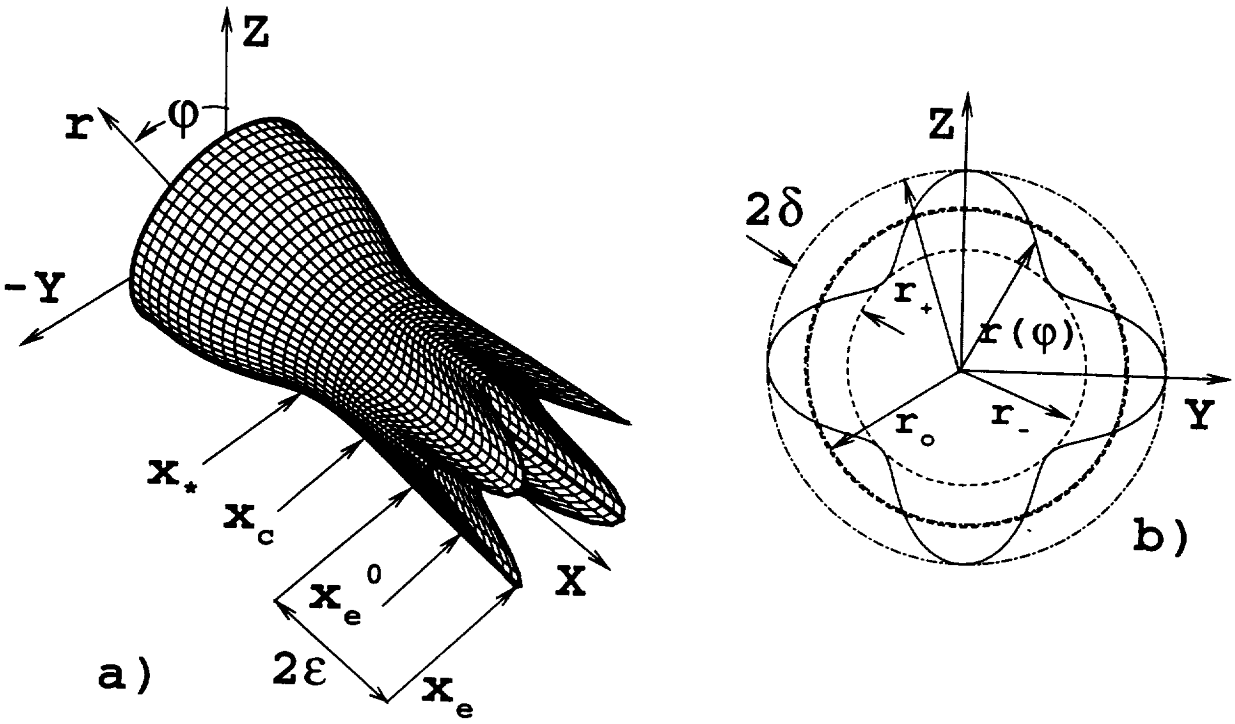

Fig.1 The Bluebell nozzle on the base of convergent-divergent round designed nozzle.

a) x,y,z-Cartesian and x, r, φ- cylindrical coordinates; $x = 0$-an inlet, x_*- a throat, x_c- a start of the sinusoidal cross section variation, x_e^o-a baseline nozzle edge, x_e-a Bluebell nozzle edge, ε-a petal amplitude coefficient. b) a cross section nozzle contour, $r_o{=}R_o(x)$- an "equivalent" round nozzle radius, $r_\pm$-maximum and minimum radius values, $\delta{=}\frac{1}{2}(r_+ - r_-)$- a corrugation amplitude coefficient, $r(\varphi)$-a cross section nozzle contour.

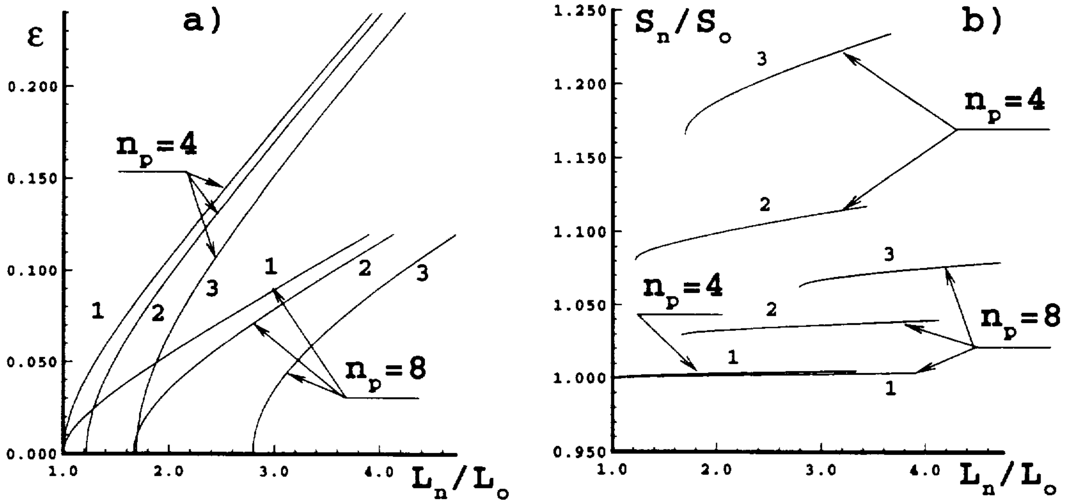

Fig.2 The ratio of the edge lip line lengths (a) and the lateral areas (b) of Bluebell (subscript index "n") and baseline (subscript index "o") nozzles vs the petal amplitude coefficient ε for the different values of the corrugation amplitude coefficient δ_o and variation frequencies $n_p = n_c = 4$ and 8. The numbers at the curves 1,2,3 are: 1 -δ_o=0, 2 -δ_o=0.25, 3 -δ_o=0.5.

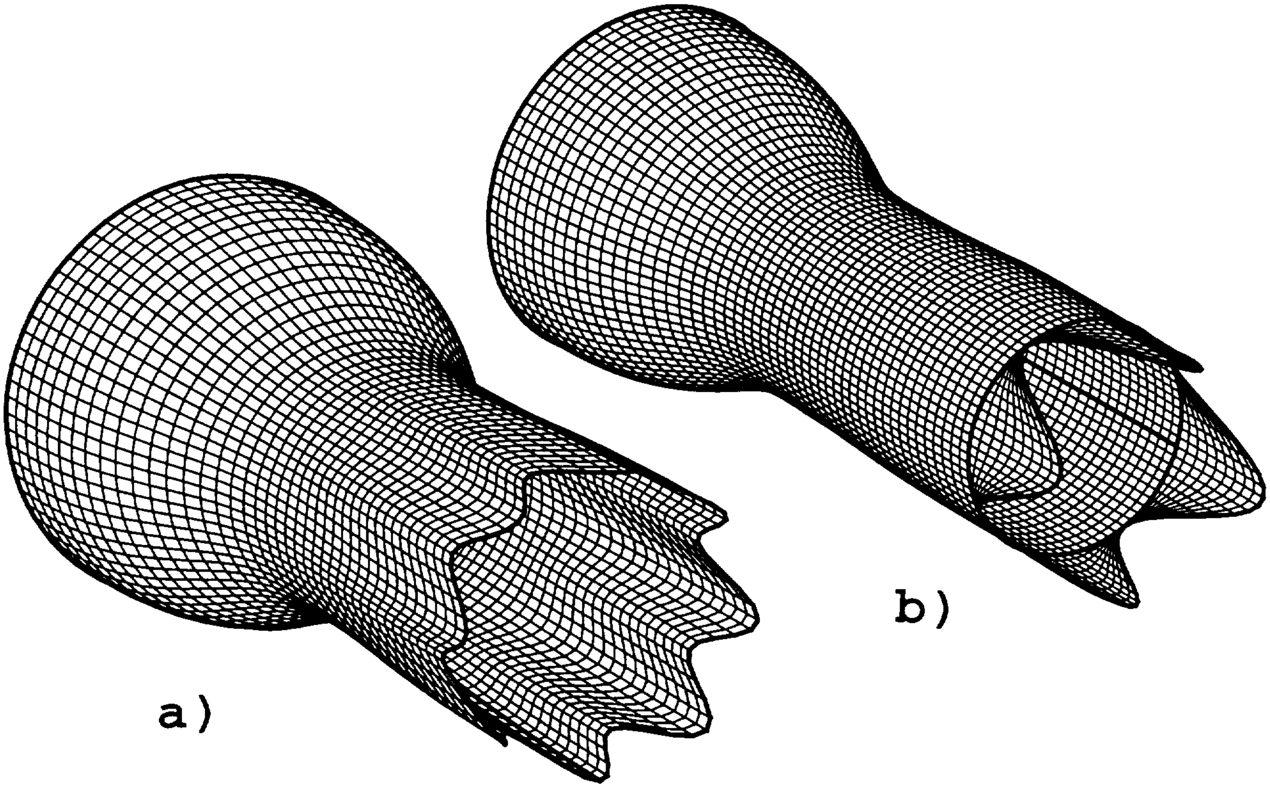

Fig.3 Two different Bluebell nozzle embodiments: **a)** - the petal middle line always locates at the exit round nozzle cross section; **b)** - with petals formed by an additional sheet to the baseline round nozzle and a minimal distance to the nozzle edge always larger than the round nozzle length.

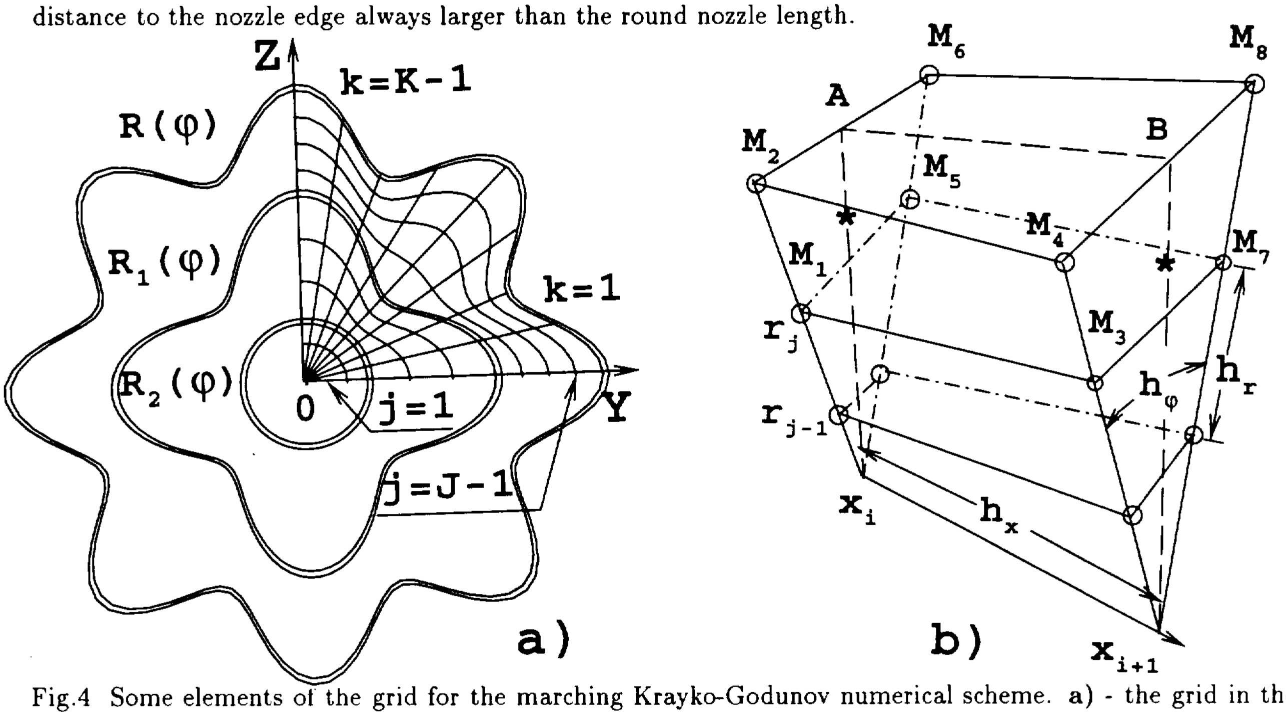

Fig.4 Some elements of the grid for the marching Krayko-Godunov numerical scheme. **a)** - the grid in the cross section $x = x_i$; **b)** - the neighbor six-side cells in the cylindrical coordinate system.

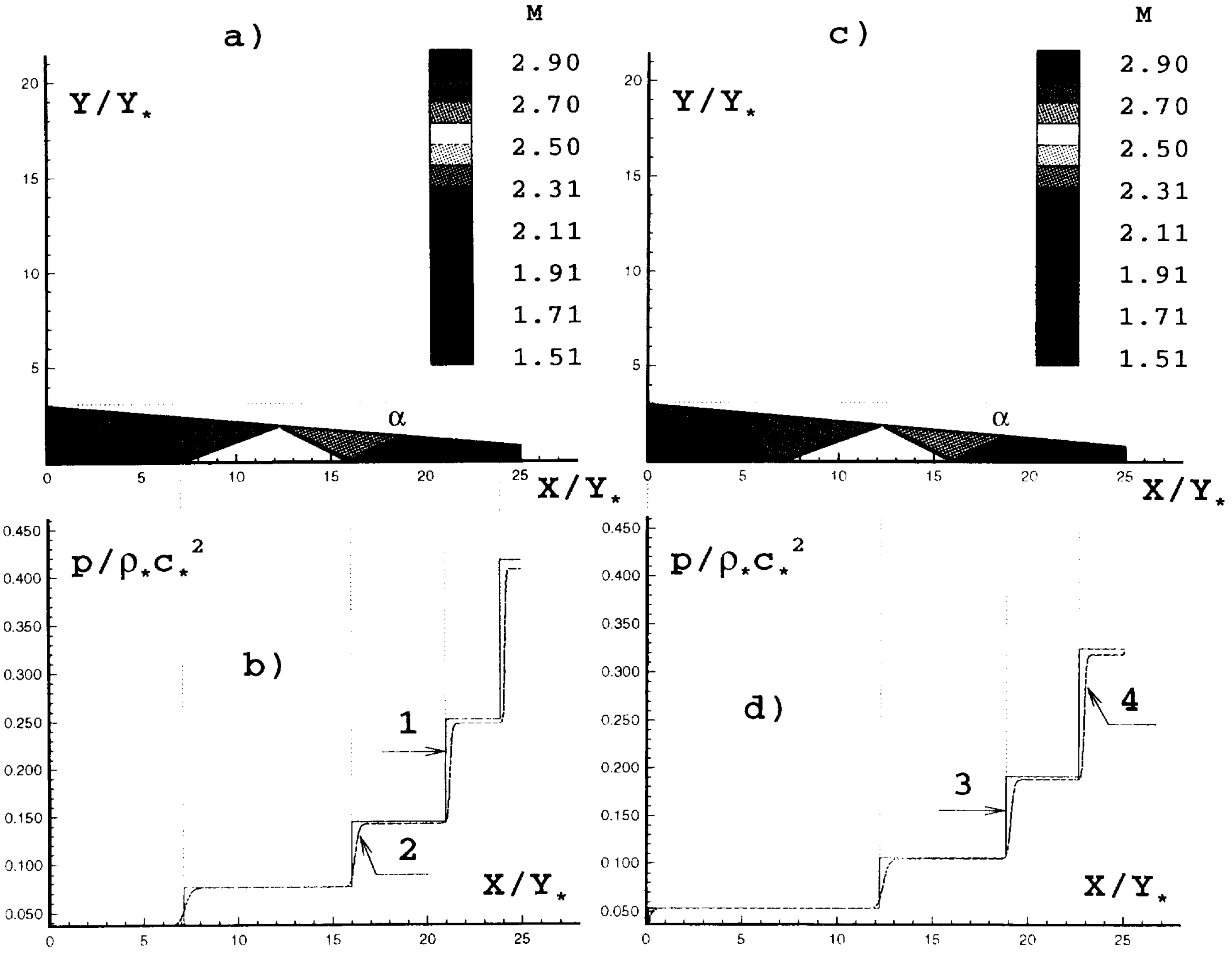

Fig.5 The comparison of the numerical and exact solutions for a supersonic flow with M_∞=3 into 2D wedge-shaped inlet with the wedge angle $\alpha = 5°$; X-direction is along the wedge, Y-direction is perpendicular to X-direction; Y_*= Y value at nozzle throat. The nondimensional step in Y-direction h_y=0.01. **a)** Mach contours; **b)** pressure distribution along the plane of symmetry: 1-exact solution, 2- numerical solution; **c)** Mach contours (the same as in a)); **d)** pressure distribution along the wall: 3-exact solution; 4-numerical solution.

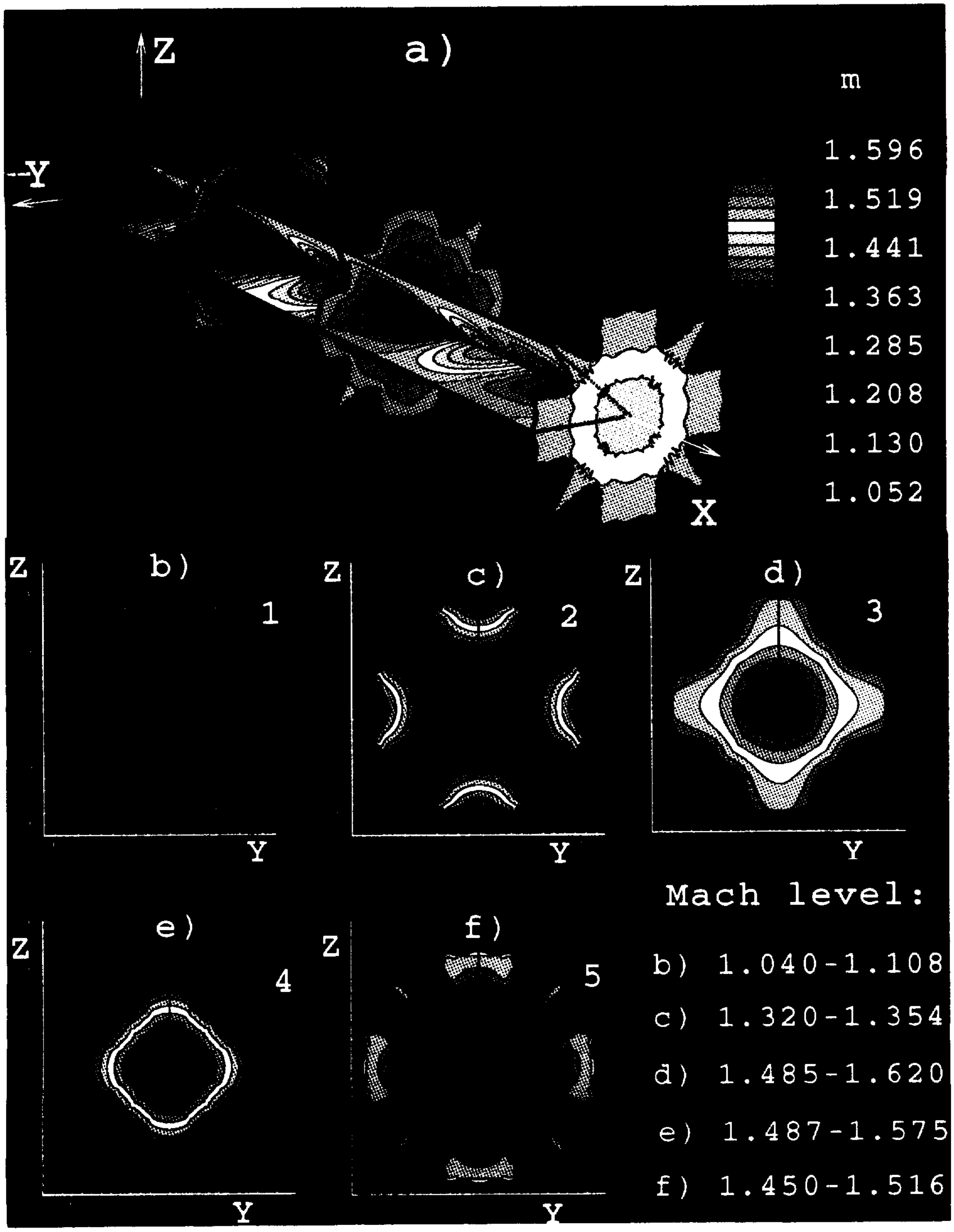

Fig.6 Mach contours in the planes of symmetry and in five cross sections for a flow into 4-petal Bluebell nozzle with $n_p = n_c = 4$, $\varepsilon = 0.7$, $\delta_0 = 0.2$ and into exhaust jet with pressure ratio NPR=3.684 ($M_e = 1.5$); $x_e^0 = 3.27$. **a)** 3D picture. More detail 2D pictures for five cross sections are in the **b)** to **f)**. The cross section locations are: b) (1)-x=0, c) (2)-x=1, d) (3)-x=2.5, e) (4)-x=4, f) (5)-x=10.

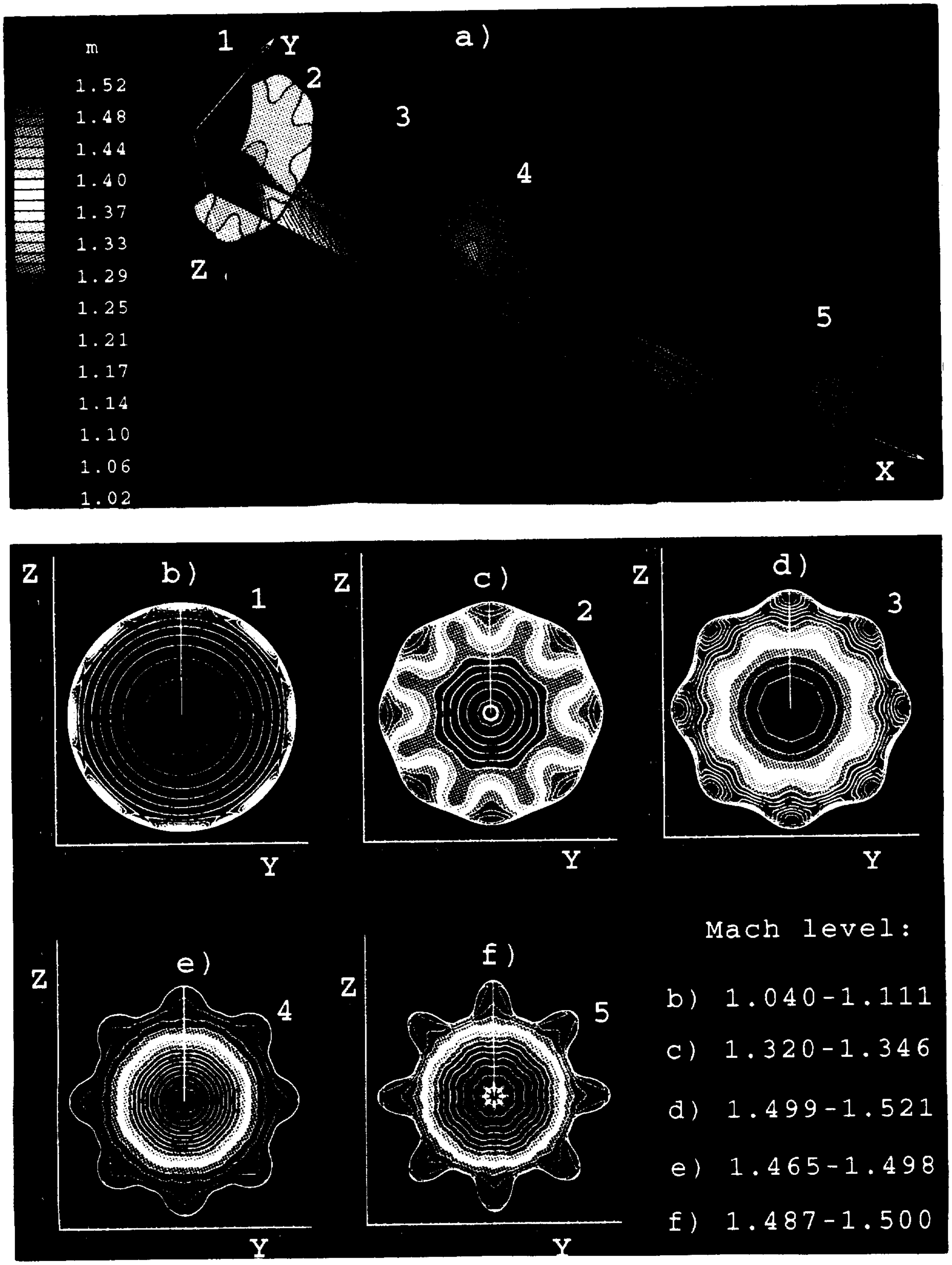

Fig.7 The same as in Fig.6, but for 8-petal Bluebell nozzle with $n_p = n_c = 8$, $\varepsilon = 0.35$, $\delta_0 = 0.2$

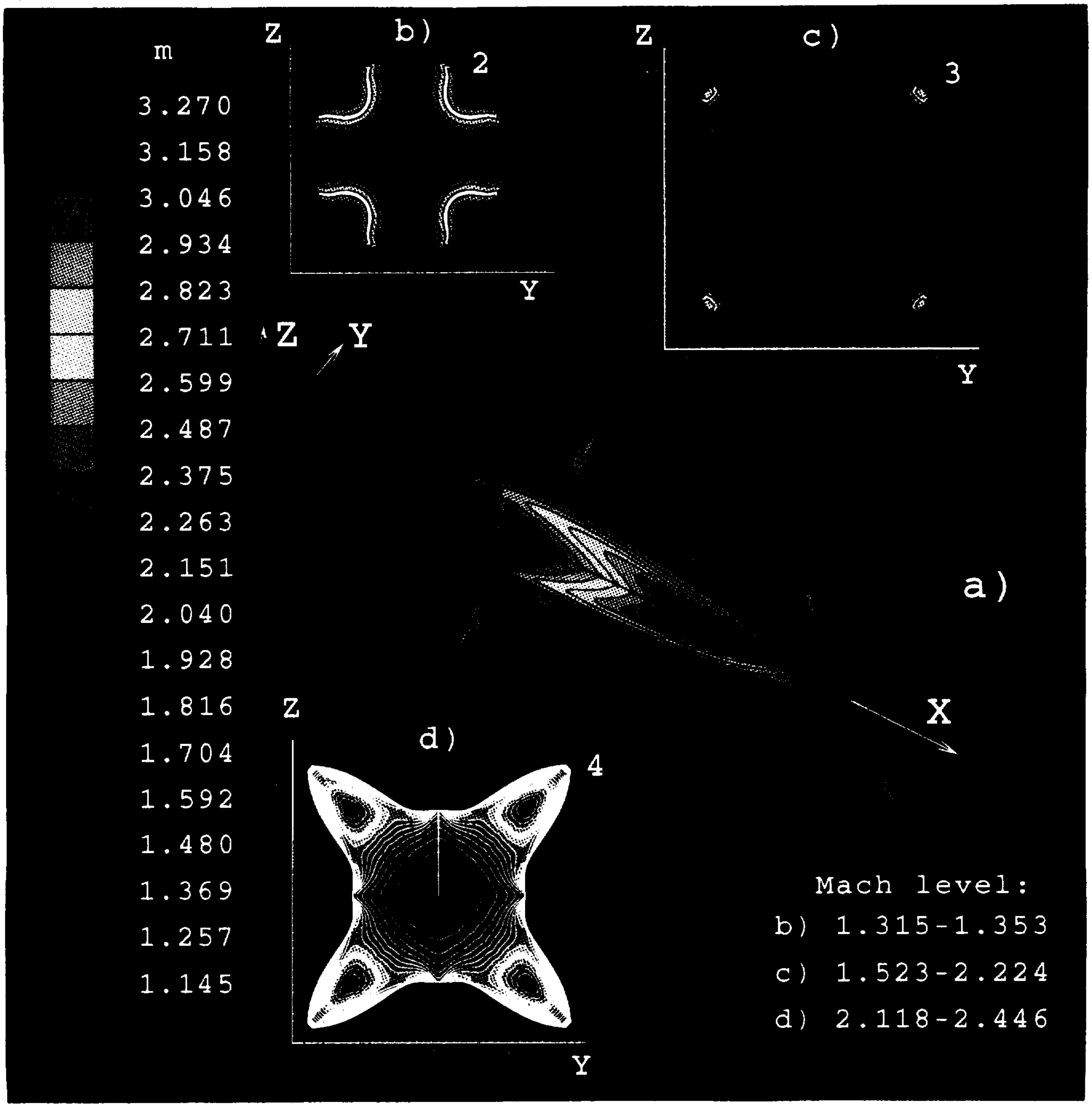

Fig.8 The same as in Fig.6, but for 4-petal Bluebell nozzle with $n_p = n_c = 4$, $\varepsilon = 0.35$, $\delta_0 = 0.2$ and underexpanded jet with pressure ratio NPR=17 (M_e=2.5).

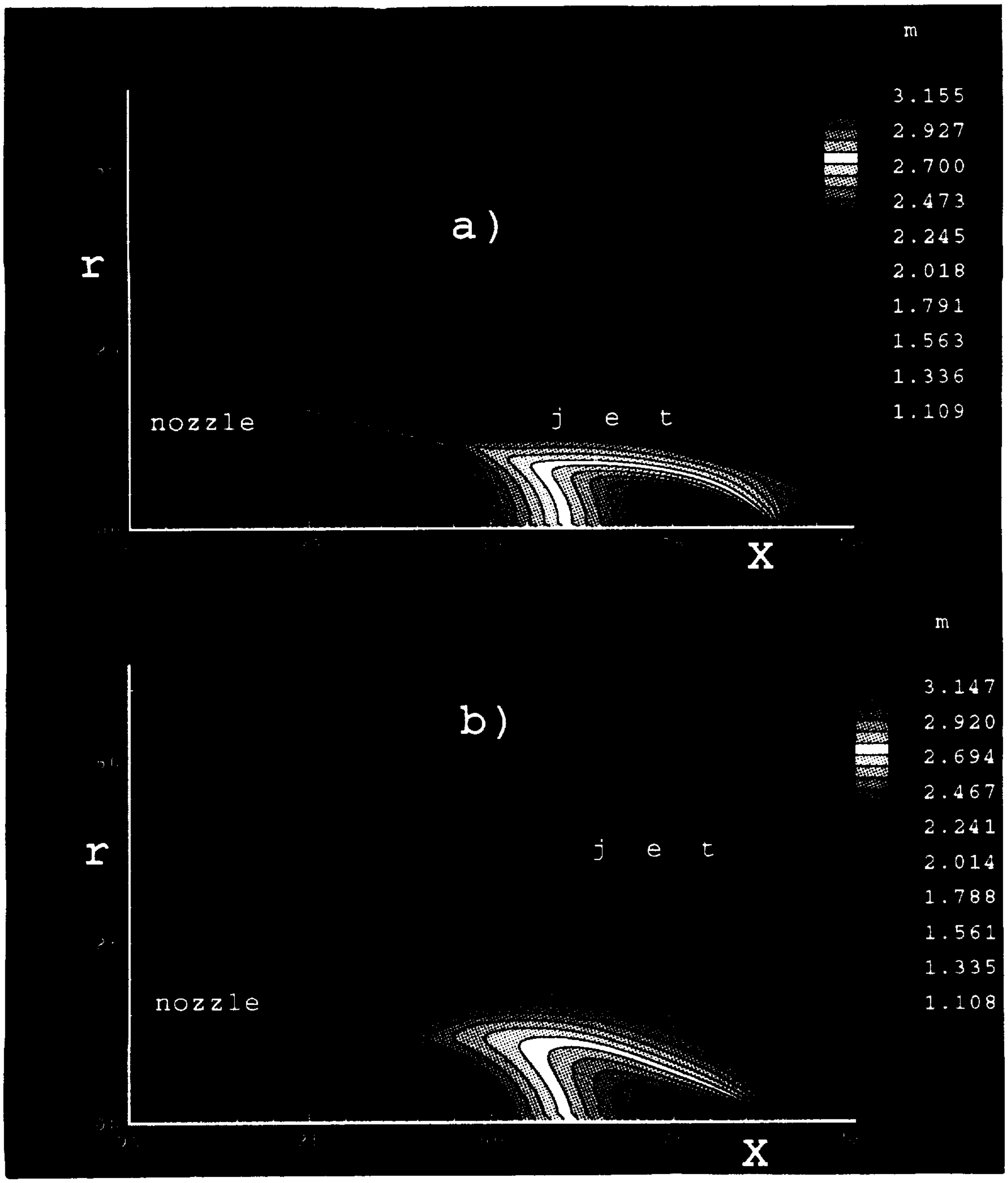

Fig.9 Mach contours in two planes of symmetry shown in Fig.8, (**a**-$\varphi = 0^\circ$, **b**-$\varphi = 45^\circ$).

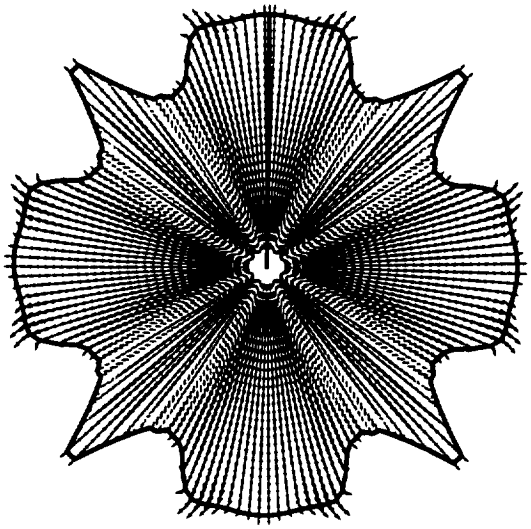

Fig.10 Velocity map in the cross section x=4 for Bluebell nozzle with geometric parameters: $n = n_p = n_c = 4$, $\varepsilon = 0.7$, $\delta_0 = 0.2$; NPR=3.684.

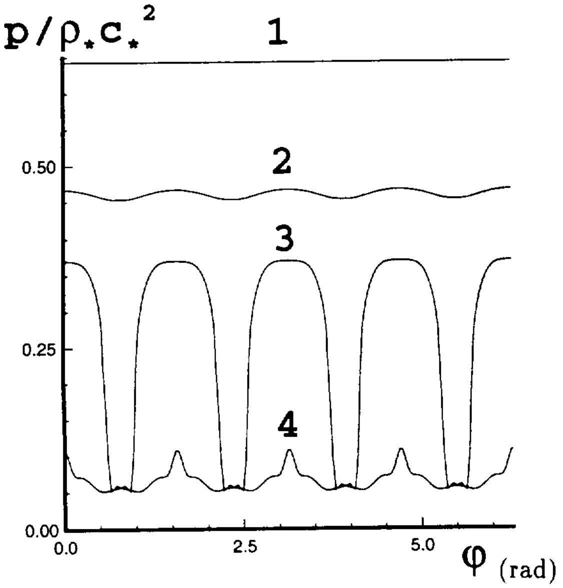

Fig.12 The *Bluebell* nozzle 1st embodiment, n=4. Underexpanded jet with M_e=2.5. Pressure distribution vs an azimuth angle φ for the different cross sections, ε=0.35, δ_0=0.2; 1-x=0, 2-1, 3-2.5, 4-4.

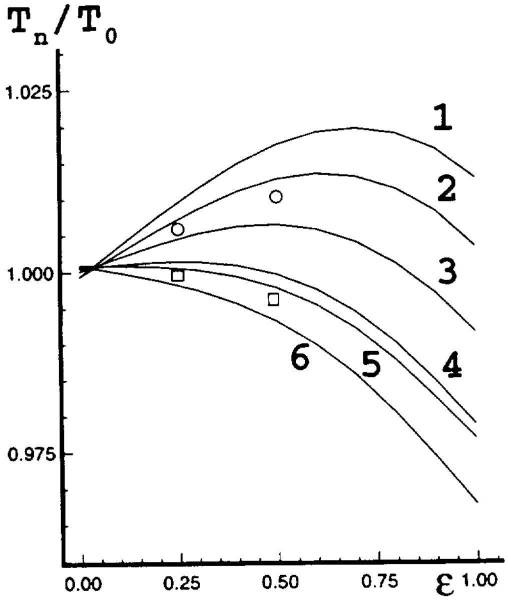

Fig.11 The Bluebell nozzle 1st embodiment, n=4. Dependence of the thrust ratio T_n/T_0 from geometric parameters ε and δ_0. T_n-the Bluebell nozzle thrust, T_0-the baseline round nozzle thrust. Inviscid Euler approximation: 1- δ_0=0.3, 2-0.2, 3-0.1, 4-0; with the boundary layer corrections: 5-δ_0=0.1, 6-0. NSE solution by CRAFT code: circle-δ_0=0.2, square-δ_0=0.

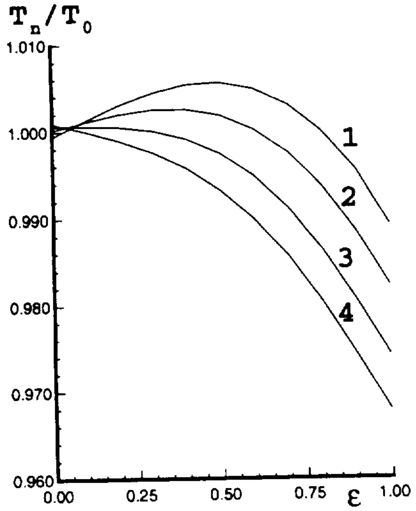

Fig.13 The Bluebell nozzle 2nd embodiment, n=4. Dependence of the thrust ratio T_n/T_0 from geometric parameters ε and δ_0 with taking into account the boundary layer corrections: 1-δ_0=0.3, 2-0.2, 3-0.1, 4-0.

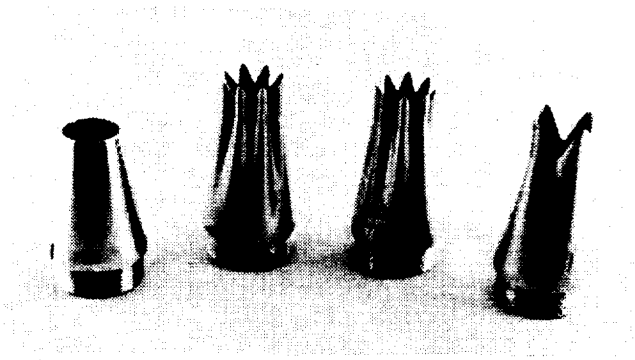

Fig.14 The Bluebell and baseline round nozzles, which were tested in the Small Anechoic Jet Facility (SAJF) at NASA Langley Reserch Center. From left to right are #9,#1,#8 and #5 nozzles.

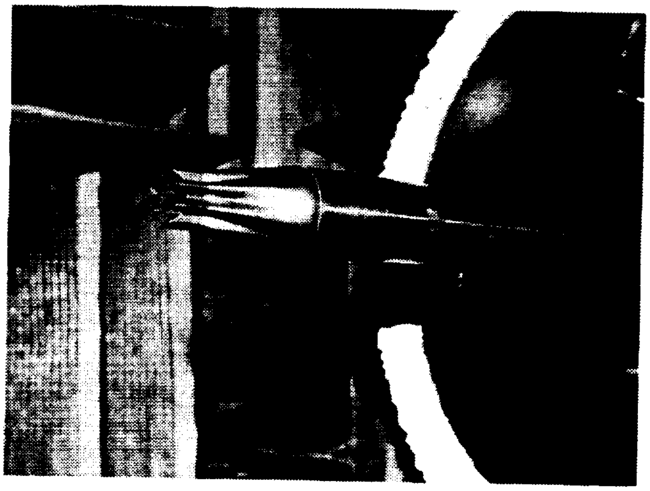

Fig.15 Existing 8-petals Bluebell nozzle mounted in the SAJF.

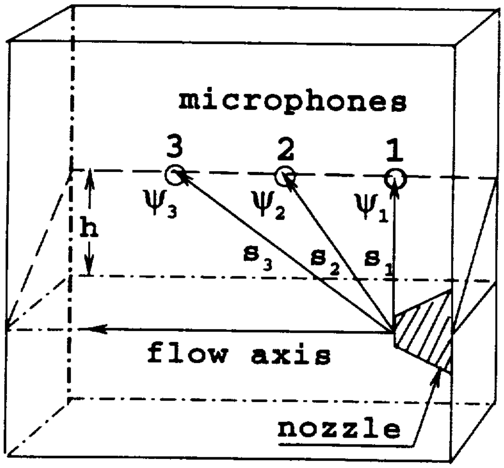

Fig.16 The sketch of the mutual location of the microphones and the nozzle-jet system. $\Psi_1 = 91.1^o$, $\Psi_2 = 125.7^o$, $\Psi_3 = 145^o$; $S_1 = 70.75''$, $S_2 = 86.125''$, $S_3 = 121.375''$; $h = 10''$.

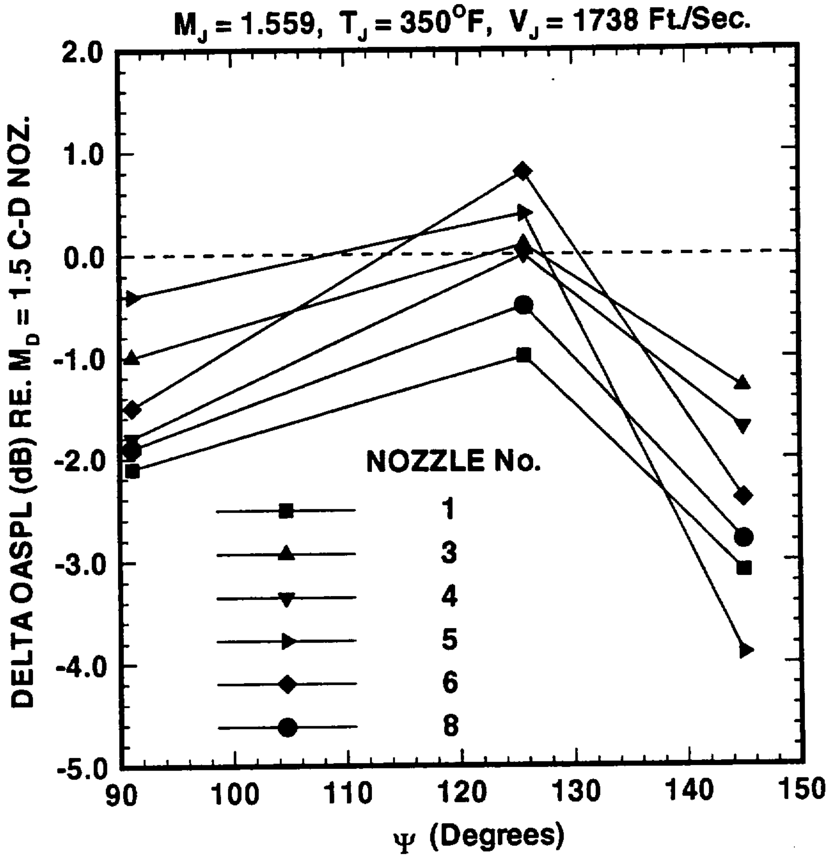

Fig.17a The supersonic condition. The overall pressure level differences of the Bluebell nozzles relative to that measured from the baseline round convergent-divergent nozzle with design exhaust Mach number $M_e = 1.5$. These values are presented vs a sound radiation angle Ψ.

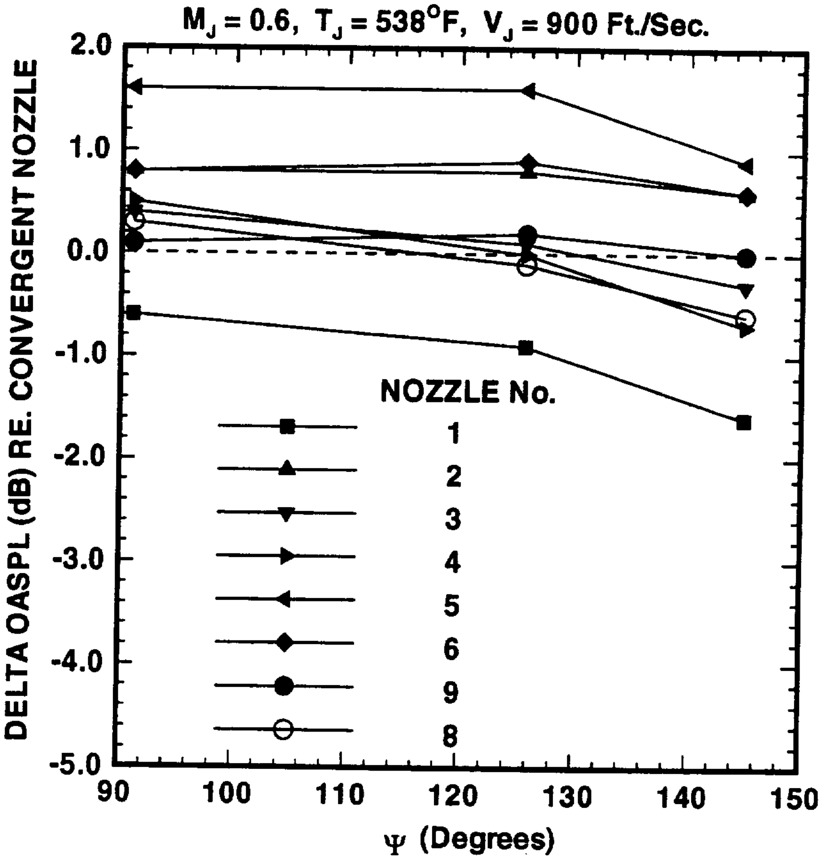

Fig.17b The subsonic condition. The overall pressure level differences of the Bluebell nozzles relative to that measured from the baseline round convergent nozzle. These values are presented vs a sound radiation angle Ψ.

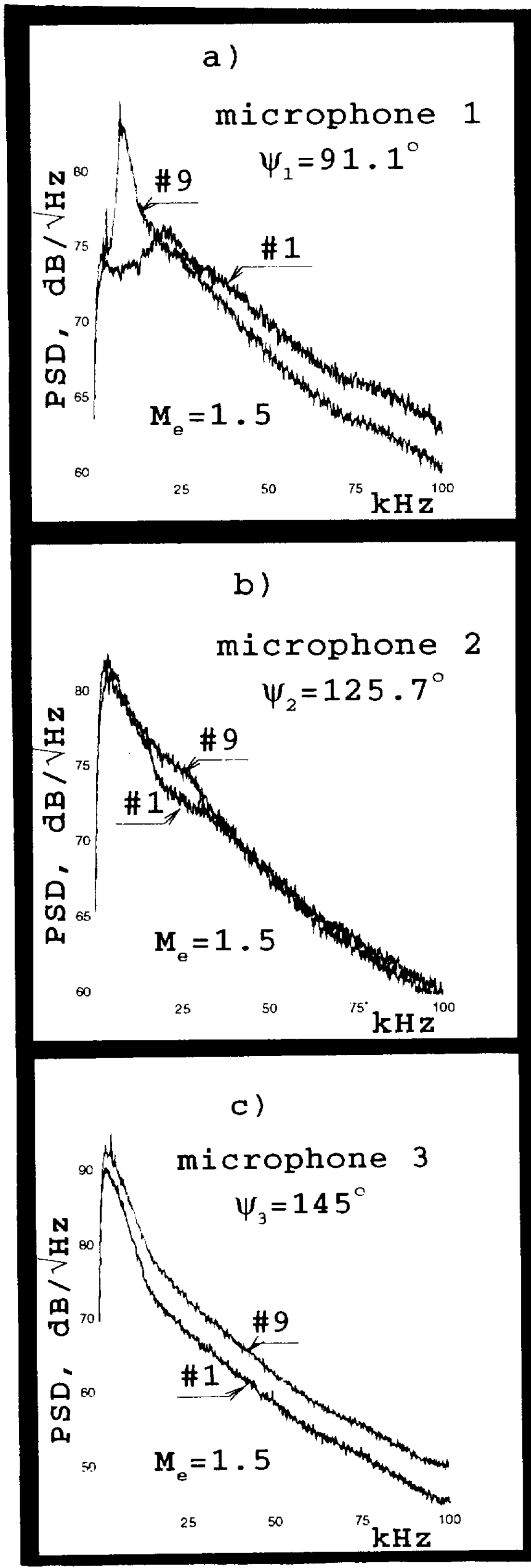

Fig.18 The supersonic condition. The acoustic power spectral density vs frequency determined by three micrphones: **a)** microphone 1 ($\Psi_1 = 91.1^o$), **b)** microphone 2 ($\Psi_2 = 125.7^o$), and **c)** microphone 3 ($\Psi_3 = 145^o$).

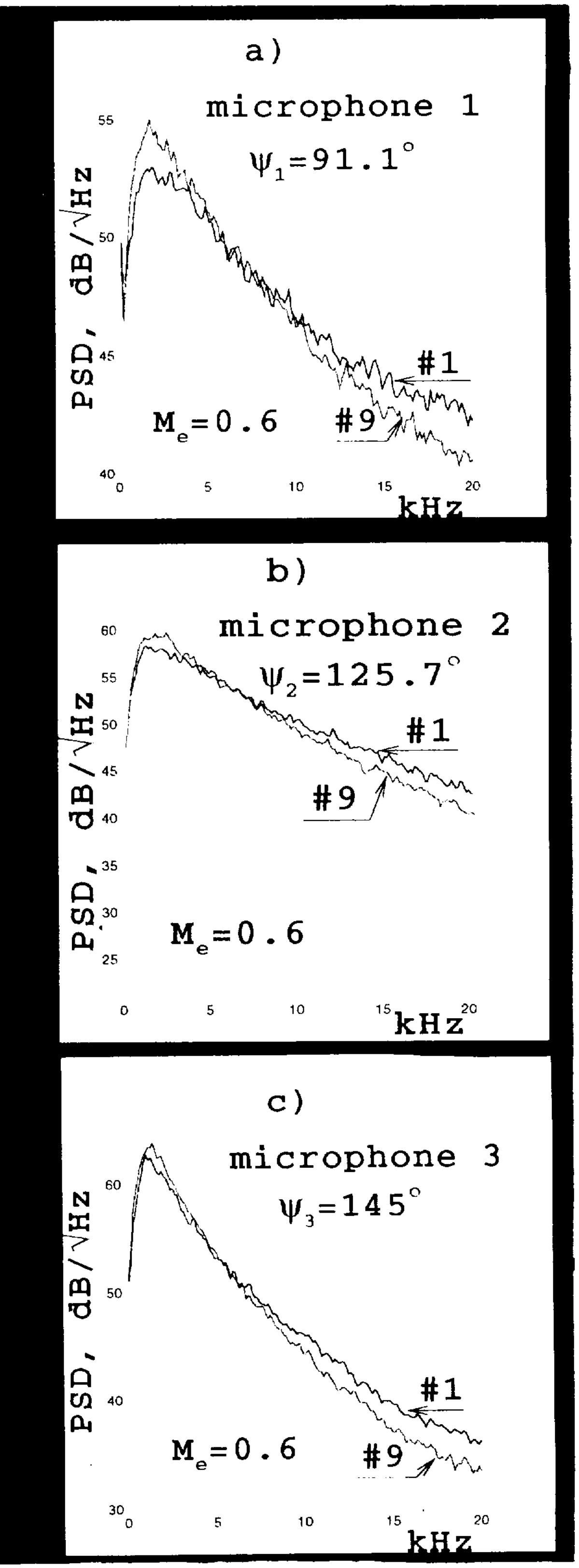

Fig.19 The subsonic condition. The acoustic power spectral density vs frequency determined by three micrphones: **a)** microphone 1 ($\Psi_1 = 91.1^o$), **b)** microphone 2 ($\Psi_2 = 125.7^o$), and **c)** microphone 3 ($\Psi_3 = 145^o$).